

Rock toppling failure mode influenced by local response to earthquakes

Zelin Zhang^{1,2} · Tao Wang¹ · Shuren Wu¹ · Huiming Tang²

Received: 30 March 2015 / Accepted: 22 September 2015 / Published online: 3 October 2015
© Springer-Verlag Berlin Heidelberg 2015

Abstract Earthquake waves influence rock toppling stability, and the effects of local earthquake propagation and topographic also affect slope deformation. Detailed engineering geology conditions of slopes are obtained and a geomechanical characterization of rock topplings is performed. To study the input earthquake waves and slope interactions, a dynamic analysis is performed using the UDEC 4.0 discrete element method (DEM) numerical code under viscoplastic conditions. The earthquake signals are representative of different peak ground acceleration, Arias intensities, and frequencies, and are used in the study of different rock topplings with different height, slope angle, and strata dip angle. The derived outputs are processed for the earthquake propagation study and to assess the induced deformation mechanisms in terms of resulting displacements, plastic zone features, and deformation mode. The results prove that an interaction exists between stratigraphic and topographic effects on earthquake wave propagation, and that these effects cannot be assessed independently. The obtained results describe the effect of topography and geological settings in rock topplings, amplifying or de-amplifying earthquake ground motion, and demonstrate that the tensile state dominates at the slope surface but evolves with depth. A shear state dominates at the toe or in the deep part of rock topplings. The rock toppling deformation mode may develop into a composite of tension fractures at the crest and

sliding at depth. Compared with the static scenario, under earthquake load, tensile deformation evolves over a larger area at the crest and develops a shear zone at the toe and in the substrata. The necessary earthquake-induced toppling conditions are discussed, and the UDEC 4.0 DEM method and conventional pseudostatic approach are compared. This study shows there are a broader range of deformations inside the slope.

Keywords Toppling · Earthquake response · Peak acceleration PGA · Discrete element method · Failure mode

Introduction

Earthquake-induced slope instabilities are often responsible for the greatest damage and losses during earthquakes (Bird and Bommer 2004; Chigira et al. 2010; Bozzano et al. 2011). Slope instabilities have been documented in historical earthquakes such as the 1976 Friuli (Italy) earthquake, the 1985 Chile earthquake, the 1999 Chi-Chi (Taiwan) earthquake, and the 2008 Wenchuan (China) earthquake. In the last few years, some specific case studies have focused on reconstructing the mechanisms of landslides and deterministic prediction of earthquake-induced ground failure scenarios (Wasowski and Del Gaudio 2000; Martino and Mugnozza 2005; Chigira et al. 2010; Bozzano et al. 2011; Pal et al. 2012).

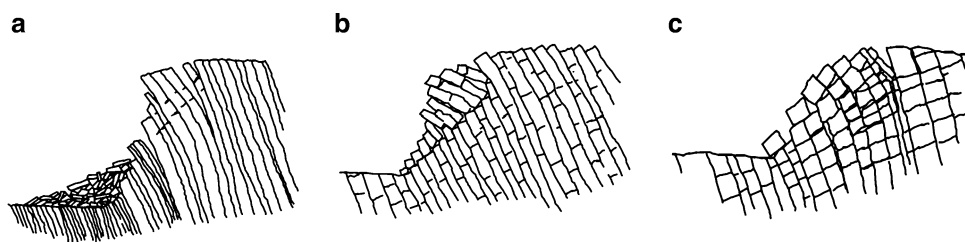
Among the various possible rock slope failure mechanisms, toppling is of particular interest because toppling movements range from slow to extremely rapid (Nichol et al. 2002). Goodman and Bray (1976) recognized three types of toppling failures: flexural, block, and block-flexural. In these three types, the main set of joints dip into the

✉ Tao Wang
wangtao_ig@163.com
Zelin Zhang
249133236@qq.com

¹ Institute of Geomechanics, Chinese Academy of Geological Sciences, Beijing 100081, China

² China University of Geosciences, Wuhan 430074, China

Fig. 1 Toppling modes observed in the field: **a** flexural toppling, **b** block toppling, **c** block-flexural toppling (Alzo'ubi et al. 2010; Zhang et al. 2015)



slope. Figure 1 illustrates the three types of toppling. A common feature of all modes is the eventual development of a rupture surface (Alzo'ubi et al. 2010; Zhang et al. 2015). Despite extensive studies on static toppling (Pritchard and Savigny 1990; Alzo'ubi et al. 2010; Bobet 1999; Scholtès and Donzé 2012; Zhang et al. 2015; Moh-taramin et al. 2014; Babiker et al. 2014), very few studies have been done on toppling failure under dynamic loads. Recently, possible interactions between earthquake waves and slopes have been discussed to forecast earthquake-induced slope instabilities to show how slope mechanisms and influencing factors depend on earthquake input properties such as energy, frequency content, directivity, and peak ground acceleration (PGA) (Ashford et al. 1997; Rathje and Bray 2000; Saygili and Rathje 2008; Lenti and Martino 2012, 2013; Rizzitano et al. 2014). Earthquake propagation effects on slopes can be evaluated by engineering geology models through vibration centrifuge tests, numerical simulation, and Newmark's method (Romeo 2000; Lenti and Martino 2012; Rizzitano et al. 2014; Kokusho et al. 2014; Jiao et al. 2014). These studies suggested that surface topography, slope height, and stratigraphy modify earthquake ground motion. Topplings usually toppled progressively under static loads. The bottom strata were damaged first, and formed free surfaces that caused the overburdened strata to be dumped gradually. The extent of damage is usually focused on the slope surface, and it is difficult to produce a wide range of damage. But under dynamic load, with the earthquake input, a larger range of internal slope failure may develop. A previous study (Zhang et al. 2015) explored the evolution of topplings and discussed the plasticity zone and failure mode in such slopes.

Although previous researchers have quantitatively or semi-quantitatively analyzed the dynamic processes of many landslide types, knowledge of toppling slopes is unclear in some respects. For example, what is the relationship between the condition under which failure could occur and the frequency range, amplitude, and direction of earthquake waves for toppling slopes with different strata dip angles and slope angles? What are the influences of complex mountain massif conditions on toppling? Quantitative studies of these issues are seldom reported in the current literature.

In this regard, based on the authors' previous study in a hydropower station (Zhang et al. 2015), the UDEC 4.0 discrete element study method (DEM; Itasca 2004) presented here is focused on interactions between earthquake inputs and toppling slopes to evaluate the possible role of earthquake wave propagation and to quantify the induced deformation-failure mechanisms. The study has some practical engineering significance as a reference for the construction of predictive scenarios of earthquake-induced slope movements.

Toppling

The Cihaxia hydropower station is located in a deep valley of the Yellow River, in northeastern Qinghai-Tibetan Plateau, northwestern China. Under study are the elevation of the valley floor that is about 2740–2760 m asl and the top of the slope is at over 3090 m asl, with relative relief of about 350 m. The left bank is a dip slope with alternating steep and gradual steps. The general slope angles are 45°–65°. Here, mountains are high with outcrop. The valley is deep and V-shaped, and the river is 100 m wide with a small number of river terraces. The slope strata are mainly Middle Triassic in age (T_2). The rock mass comprises alternating layers of soft slate and hard sandstone in three combinations: (1) pale jade-green (celadon) sandstones intercalated with gray slates ($T_2 - S1 + Ss$); (2) mostly moderate thin sandstones with slates ($T_2 - Ss$); and (3) gray laminar slates intercalated with 0.5–10 cm thick, weak, and weathered sandstone ($T_2 - S1$). The Triassic strata form a homocline trending 325°–355° (average 340°) and dipping 62°–80° (average 74°). The overlying 10–50 m strata are Pleistocene (Q_3^{al+pl}) and Holocene (Q_4^{col} , Q_4^{dl}) in age. The deformed slope is 1 km long, 350–400 m high, and in the left riverbank with reversed strata. The upper slope is at 3100 m asl with an angle of 41°–46° (locally 62°–80°). Site investigation, exploration adit, and borehole logs documented the presence of poorly developed joint sets (Fig. 2; Zhang et al. 2015). Here we observed three types of toppling.

The dip angle of the surface strata decreased with increasing vertical elevation. Above 2950 m asl, the dip

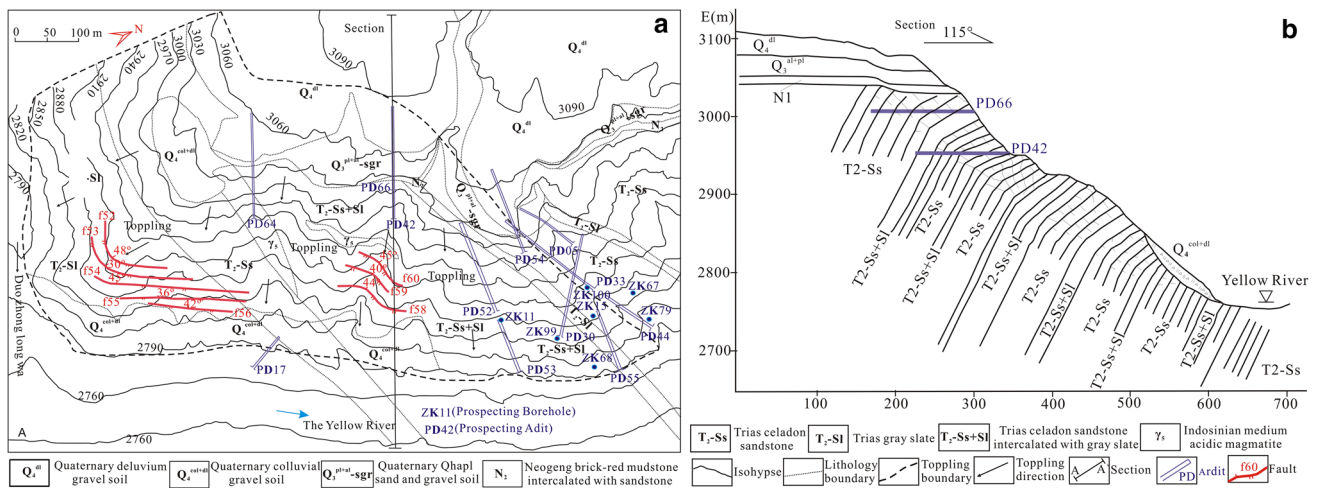


Fig. 2 a Geology map of the study area; b engineering geological profile

angle is less than 30°, and strata topple severely. In the middle part, the extent of toppling decreases with decreasing elevation, but below 2820 m asl, it turns normal. On the crest, deep toppling tension cracking and surface block toppling failure are dominant, whereas deep flexural deformation and local shallow failure are dominant in the lower slope. The contact relation between deformed and intact strata is transitional between the flexural deformation of the slate and the fracturing of the sandstone. At the same elevation, the surface strata show severe toppling and gradually weaken towards horizontal depth inside the hill mass. The dip angle of the upper slope strata change with the inward length in the adits. The dip angle is <30° or nearly horizontal within 25 m from the entrance and less than 50° at 60–80 m from the entrance; beyond 80–90 m from the entrance, the dip angle increased gradually to 78°–82°. The strata incline NE facing the Yellow River as the inward length of the adits increase. At the entrance, it is NNW and 335°–350° at the bottom of the adits. The surface strata toppled before the interior.

DEM numerical modeling and earthquake inputs

To assess earthquake propagation effects due to slopes in terms of geometry and geologic setting, preliminary numerical modeling was performed on 12 different slope configurations, and different inputs were then applied to force them toward deformation and failure processes. The considered original slope lithology was sandstone and slate. The generalized slope angle $\alpha = (30^\circ, 45^\circ, 60^\circ)$, and the strata dip angle $\beta = (30^\circ, 45^\circ, 60^\circ, 75^\circ)$ (Fig. 3). These geologic settings can be regarded as being prone to toppling according to a conventional finite slope model. The

earthquake inputs for numerical modeling were selected on the basis of energy (i.e., Arias intensity) and frequency criteria (i.e., spectral acceleration, Bray et al. 1998). Following a methodology in China Chinese Standard for earthquake classification, three inputs for earthquake waves were obtained (Fig. 4). The selection relied on the acceleration records of the May 12, 2008 Wenchuan earthquake ($M_s = 8.0$, Fig. 4a, Arias intensity = 0.68), the April 20, 2013 Lushan earthquake ($M_s = 7.0$, Fig. 4b, Arias intensity = 0.45) and the July 22, 2013 Minxian earthquake ($M_s = 6.6$, Fig. 4c, Arias intensity = 0.28) which are available from the China Earthquake Administration.

The selected slope configurations are named with a code that reported the number of earthquake waves, slope angle and the dip angle of geological strata, if present (i.e., Wenchuan_30_30; Lushan_45_45; Minxian_60_60, and so forth).

The numerical analyses were performed using DEM with UDEC 4.0 code (Itasca 2004). Because the presented study mainly discusses the role of slope geometry and geological setting (strata dip angle) on the interaction between earthquake inputs and slope, no parametric study was performed for constitutive laws and parameter values. Viscous boundary conditions are imposed to absorb the waves reaching the boundaries, thereby avoiding reflection of waves back into the model (Pal et al. 2012). The lateral boundary is assumed as a free boundary condition, and the bottom boundary is selected as a viscous boundary condition. Boundary conditions consist of setting all displacements in every direction equal to zero for the bottom and the lateral sides of the model. Moreover, the Mohr–Coulomb yield criterion (e.g., elastic-perfectly plastic behavior) was used to split the strain–stress domain into two sub-domains (linear and plastic). The physical and mechanical

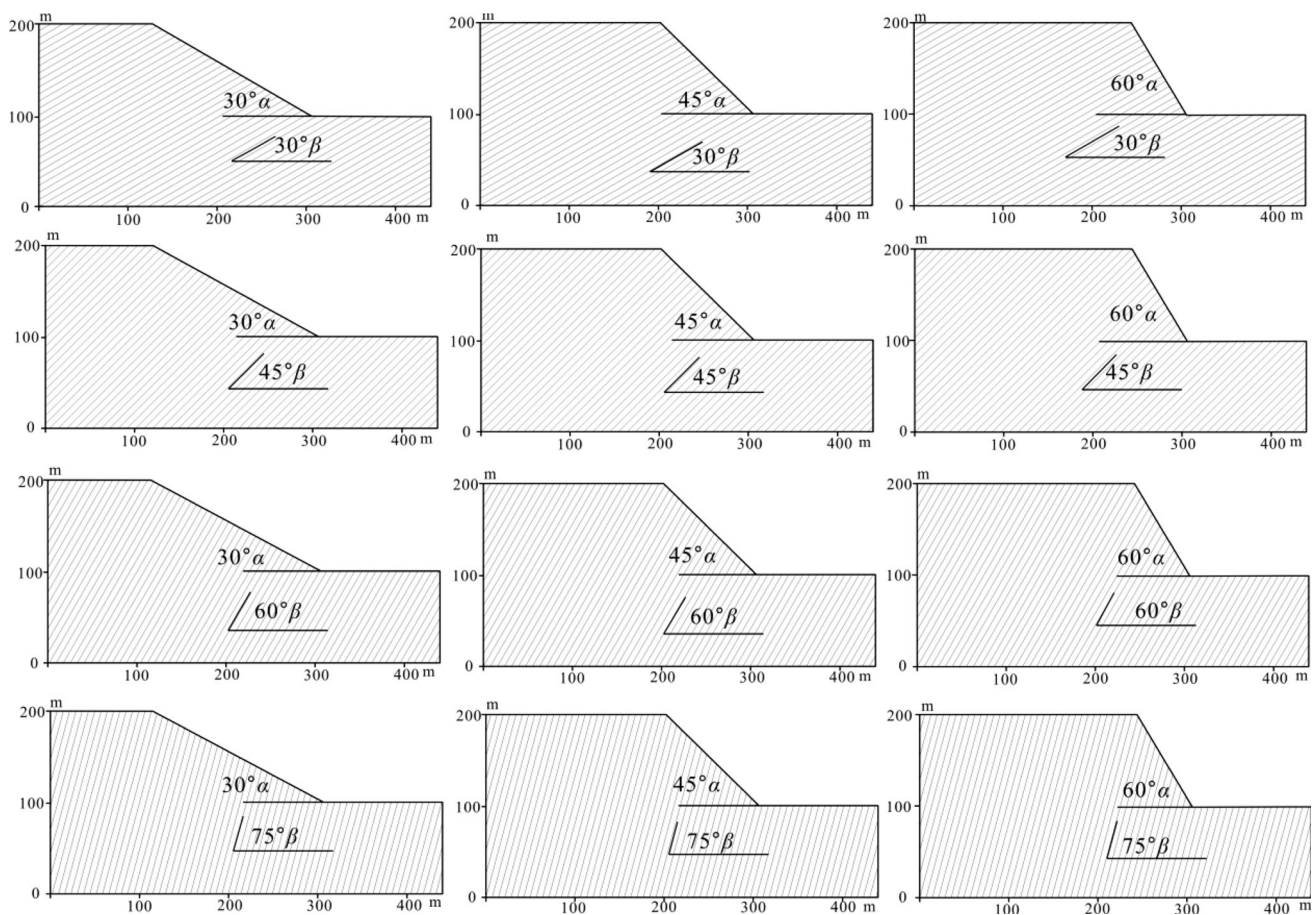


Fig. 3 Toppling configurations used for the numerical modelling

parameter values were obtained experimentally (Tables 1, 2; Zhang et al. 2015). A schematic illustration of the 2D numerical models, including the monitoring layout and boundary conditions, is shown in Fig. 5. As can be seen from the normalized acceleration response spectra for these baseline motions that presents key characteristics of these ground motions (Fig. 4d), the three earthquake waves vary within the frequency range of interest 0–10 Hz. Thus, energy dissipation in the analyses was computed in the system through a Rayleigh damping matrix defined as a combination of the mass and stiffness matrices through coefficients that depend on the modal damping ratio, adding a mass-dependent term to a stiffness-dependent one in the following form: $D = \alpha M + \beta K$, here, M is the mass matrix; K is the stiffness matrix; α is a constant for the mass damping, and β is a constant for the stiffness damping. This dissipation function implies a minimum angular frequency (ω_{\min}) in the form: $\omega_{\min} = (\alpha/\beta)^{0.5}$, which gives a minimum damping (ξ_{\min}) in the form: $\xi_{\min} = (\alpha/\beta)^{0.5}$ (Bozzano et al. 2011). The ω_{\min} was set equal to 2π radians (equivalent to a frequency of 1 Hz), and the minimum damping value ξ_{\min} (equal to $1/[2Q_{\max}]$ where Q is the

quality factor), varied as a function of the shear strain according to the adopted dynamic behavior of the rock mass (Lenti and Martino 2013). Acceleration peaks in the range of 0.02–4 Hz for the three earthquakes (Fig. 4d), which was also consistent with the grid resolution, according to the relation $f = V_s/10\Delta l$ (Kuhlemeyer and Lysmer 1973), a 2 m square grid was used to guarantee an accurate solution and to obtain a corresponding maximum admissible frequency for the model, where f is the maximum admissible frequency of the model, V_s is the minimum velocity of the S wave and Δl is the size of the largest mesh of the grid. The total width and height of the mesh are greater than twice the dimension of the slope to minimize the effects of wave reflections from boundaries.

Earthquake response of the toppling

To evaluate the strain and deformation characteristics induced by different earthquake inputs on the 12 slope configurations considered here, DEM numerical modeling using the UDEC 4.0 code (Itasca 2004) was performed

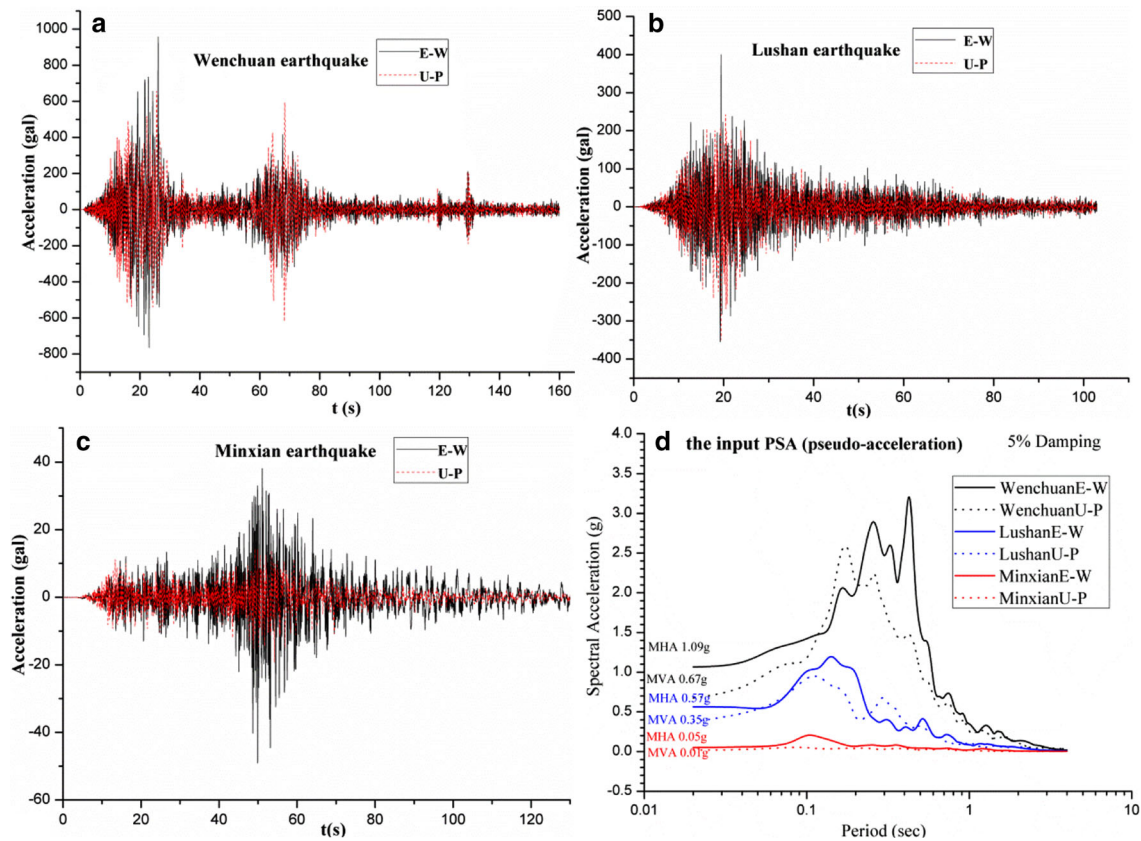


Fig. 4 Input Acceleration Time-history and response spectrum (Acceleration boundary conditions imposed at the bottom side of the model. **a** Wenchuan earthquake recorded with peak value of E-W 957.7 Gal and U-P 948.1 Gal, and the epicenter distance of the station is 18.2 km; **b** Lushan earthquake recorded with peak value of E-W

400.2 Gal and U-P 242.4 Gal, and the epicenter distance of the station is 27.7 km; **c** Minxian earthquake recorded with peak value of E-W 49.1 Gal and U-P 19.4 Gal, and the epicenter distance of the station is 134.7 km; and **d** the acceleration spectrum levels)

Table 1 Discrete element simulation parameters of rock mass

Rock property	Density (kg/m ³)	Bulk modulus (GPa)	Shear modulus (GPa)	Cohesion (MPa)	Friction angle (°)	Tension strength (MPa)	Dilation angle(°)
Toppling rock	2650	3.3	1.2	0.8	36	0.07	0
Bed rock	2700	10	4.5	1.5	45	0.5	0

Table 2 Discrete element simulation parameters of joints

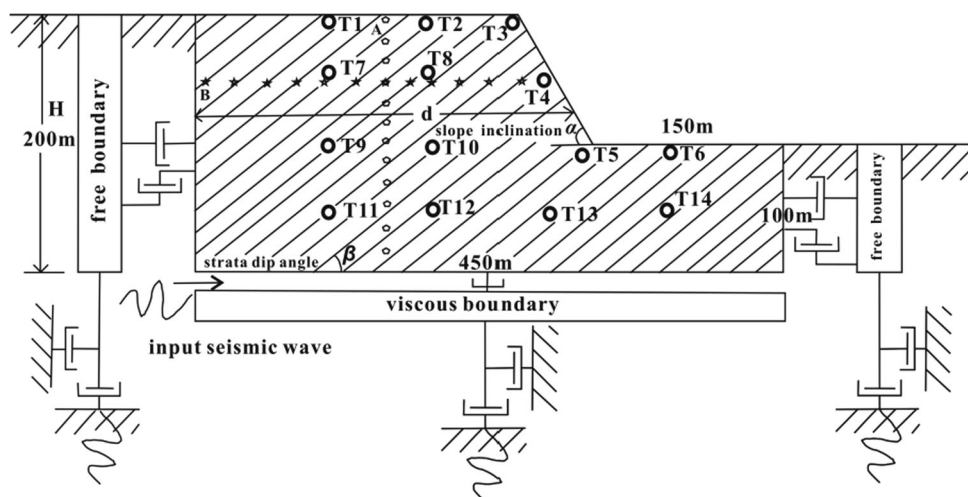
Structure property	Normal stiffness (MPa/m)	Tangential stiffness (MPa/m)	Cohesion (MPa)	Friction angle (°)	Tension strength (MPa)	Dilation angle (°)
Slate bedding	1.2	5	0.002	20	0.001	0
Superiority joint	1	4.3	0.0015	18	0.001	0

under dynamic conditions to study earthquake response of the topplings. The earthquake response of topplings obtained from the performed numerical analyses can be summarized as acceleration propagation characteristics and displacement response features.

Acceleration propagation characteristics of topplings

Three different natural earthquake waves were applied, as they have different PGAs and dominant frequencies. The

Fig. 5 Schematic illustration of the adopted model for the DEM numerical analyses



horizontal and vertical topographic propagation factors $xPGA$ and $yPGA$ in the strata were evaluated using the following equations (Bouckovalas and Papadimitriou 2005; Rizzitano et al. 2014):

$$xPGA = xPGA_E / PGA_C, \quad (1)$$

$$yPGA = yPGA_E / PGA_C, \quad (2)$$

where $xPGA_E$ and $yPGA_E$ are constants for peak horizontal (x) and vertical (y) acceleration as computed in the strata; and PGA_C is a constant for the peak acceleration of the free-field response at the toe of the slope.

1. Horizontal and vertical acceleration propagation factors PGA increased with increasing slope height and reached maximum values at the crest. For the case of Wenchuan_45_45, Fig. 6 shows the results in terms of PGA. The maximum horizontal acceleration propagation exceeds 4, and maximum vertical acceleration propagation exceeds 3 (Fig. 6a). The horizontal acceleration propagation effect is slightly larger than the vertical.
2. At the same elevation, the horizontal and vertical acceleration propagation factors of PGA increased from inside to the free face of the slope. For the case of Wenchuan_45_45, the maximum horizontal acceleration propagation reaches 3.8, and maximum vertical acceleration propagation reaches 3.3 (Fig. 6b). The horizontal acceleration propagation effect is slightly larger than the vertical as well.
3. Moreover, for the same slope configuration the acceleration propagation factors PGA increased with increasing earthquake Arias intensity. The slope acceleration propagation effect is much more intense for the Wenchuan Ms 8.0 earthquake (Fig. 6c).

The resulting earthquake-induced progressive failure is correlated generally with significant variations of

earthquake propagation effects on the slopes. In elastic wave scattering theory, the variation is caused by the input secondary vertical (SV) wave scattering at the crest and the decomposed congener SV wave and new P (primary) wave. A variety of waves superimpose and form a complicated earthquake wave field, and then cause the peak acceleration value to increase dramatically at the crest. The slope free face caused the incident and reflected wave superimposition, resulting in the propagation effect, and the absorption of rock damping for the incident wave attenuated. Figure 7a shows the configuration Wenchuan_45_45 at the slope height 80 m and 160 m acceleration became de-propagation. Because of the strong randomness of the input of natural earthquake waves, the acceleration propagation factor appeared nonlinear. Moreover, the two de-propagations in the configuration Wenchuan_45_45 may be caused by aftershocks of the Wenchuan earthquake in 60–70s (Fig. 4a). The acceleration propagation effect has satisfactory agreement with the shaking table test by Huang et al. (2013).

Toppling displacement response features

1. Under the same earthquake wave, the slope horizontal displacement (x) increased with increasing height (Fig. 7). The x -displacement is maximum at monitoring location T3; for slope configuration Wenchuan_45_60 it exceeds 0.35 m (Fig. 7c) and for slope configuration Wenchuan_45_30 it reaches 0.16 m (Fig. 7a). At the same height, the x -displacement increased as well from the interior to the slope face (e.g., T2 to T3, T8 to T4, and T20 to T5, Figs. 5, 7).
2. Slope horizontal displacement (x) and vertical displacement (y) both increased with increasing Arias intensity (Fig. 8a). Also, Fig. 8a shows that x -displacement is 9 cm and y -displacement is 16 cm for

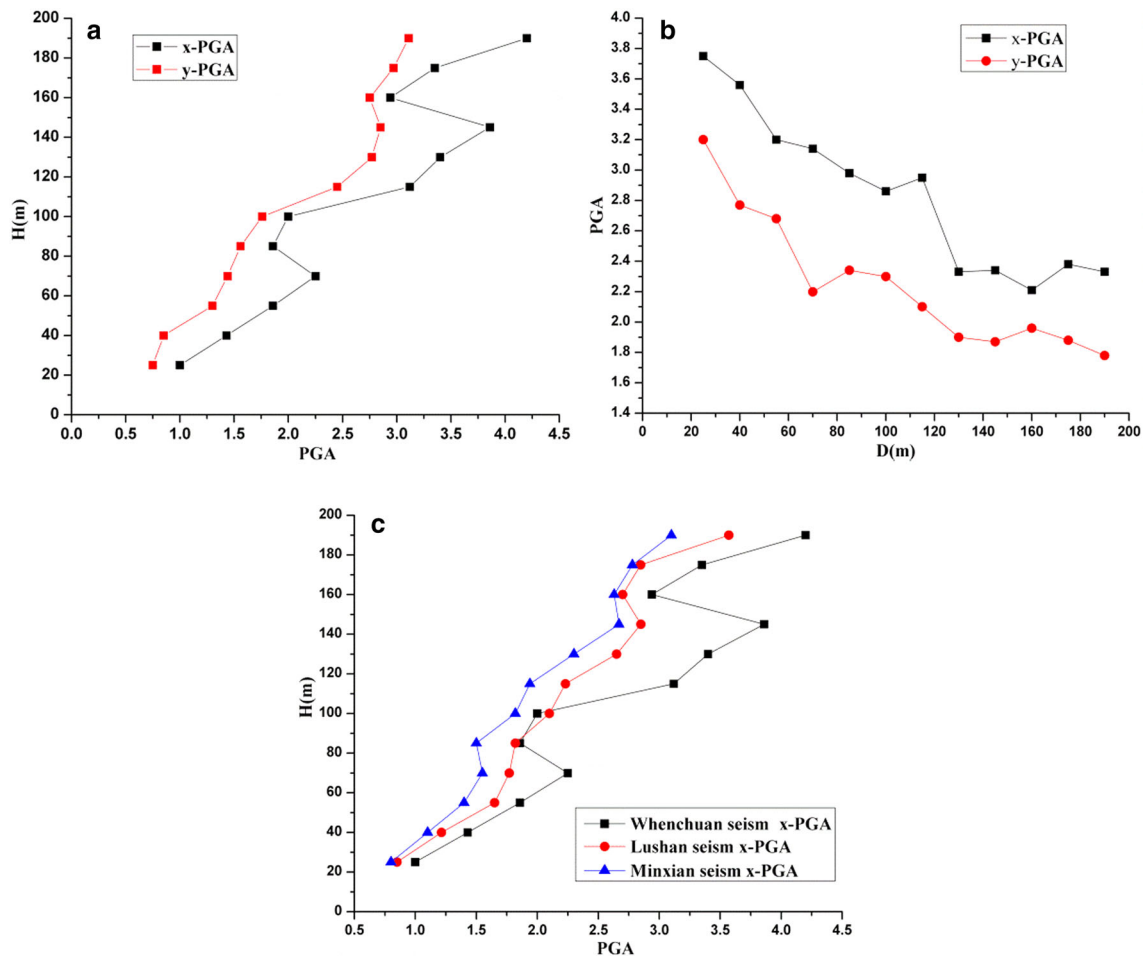


Fig. 6 Acceleration propagation effect in the slope configuration (a with the change of height, horizontal and vertical topographic propagation factors in the configuration Wenchuan_45_45; b in the same height, with the change of distance to the slope free face, horizontal and vertical topographic propagation factors in the

configuration Wenchuan_45_45; c with the change of height, horizontal topographic propagation factors in the configuration Wenchuan_45_45, Lushan_45_45 and Minxian_45_45. The monitored points are column A and row B in Fig. 5)

monitoring location T5 in the slope configuration Wenchuan_45_30. In the toppling, the vertical displacement is much larger than in the horizontal displacement. This is consistent with the static state. Toppling vertical displacement is often greater than horizontal displacement owing to bending and deformation that usually occurs under gravity. This has been proven in previous research (Goodman and Bray 1976; Pritchard and Savigny 1990; Nichol et al. 2002; Alzo'ubi et al. 2010; Zhang et al. 2015).

3. The slope horizontal displacement (x) increased with increasing strata dip angle. Figure 8b shows that the x -displacement is 10 cm at monitoring location T5 for slope configuration Wenchuan_45_30; for configuration Wenchuan_45_60 and configuration Wenchuan_45_75 the x -displacement is 30 cm at the same location. Our previous study (Zhang et al. 2015) under a static state proved that the probability of toppling

increases gradually with increasing dip angle when the strata dip angle exceeds 45° .

4. The slope horizontal displacement (x) increased with increasing slope angle (Fig. 8c). Moreover, Figs. 7 and 8 show that with the input earthquake loads, the slope displacements increased gradually. This information illustrates that with increasing earthquake motion energy, the slope displacement accumulates gradually, and permanent displacements occur in some parts of the slope.

Earthquake-induced toppling failure

To analyze the toppling failure mechanism and failure mode under different earthquake inputs for the 12 selected slope configurations, DEM numerical modeling was performed under dynamic conditions using UDEC 4.0 (Itasca

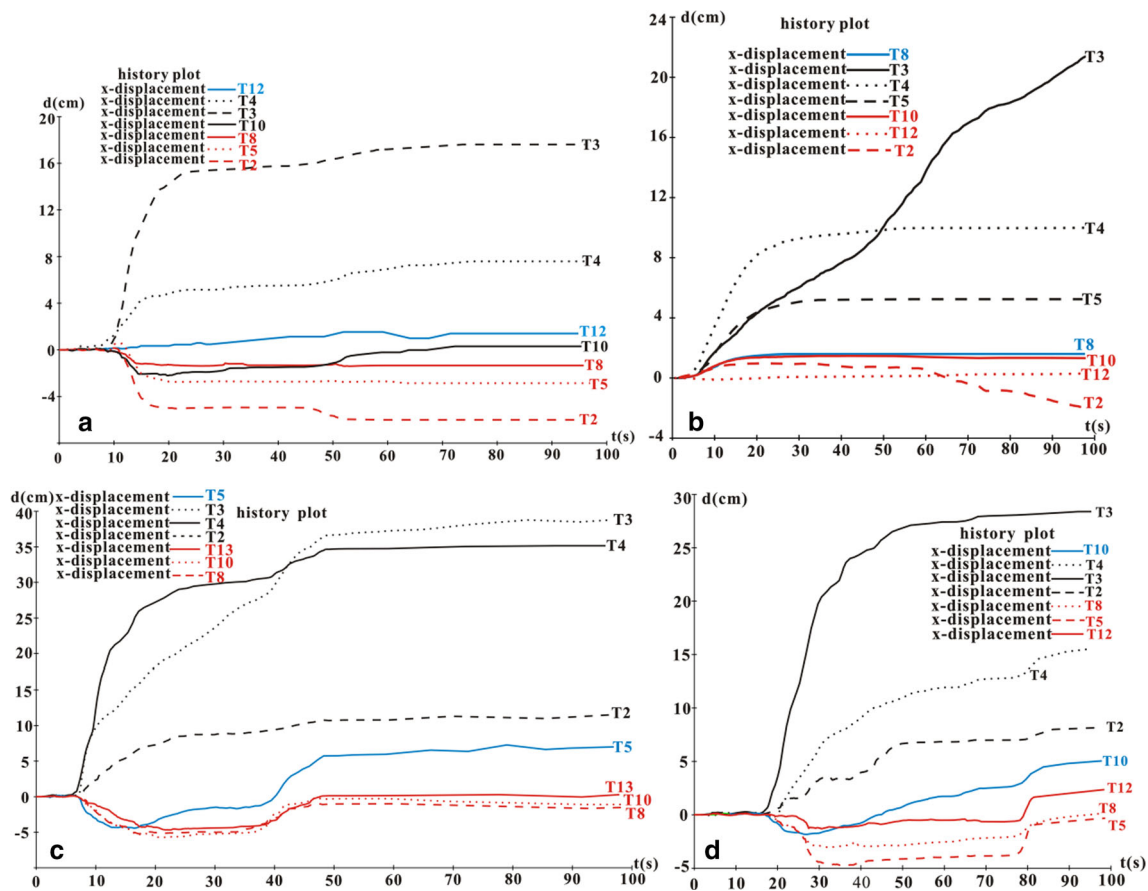


Fig. 7 Part monitoring location T2–T12 displacement history in the slope configuration (a slope configuration Wenchuan_45_30; b slope configuration Wenchuan_45_45; c slope configuration Wenchuan_45_60; d slope configuration Wenchuan_45_75)

2004). In particular, the 12 slope configurations under the Wenchuan earthquake scenario were selected for this analysis. The input earthquake wave was applied once with its time history.

Plastic zone characteristics

Figure 9 shows the plastic zone results obtained for the 12 slope configurations; these results indicate the tensile failure zone evolved mainly behind the crest of the slope, deepening with increasing slope angle and strata dip angle. From the area behind the crest to the slope face field, the tensile state dominated. For the 45° slope angle, the tensile state zone is smaller and occurs at the surface of the crest, while for the 30° and 60° slope angles, the tensile state areas range widely and produce widespread damage. Meanwhile, a shear plasticization zone evolved at the toe or in the deep part of the slope (Fig. 9a–l). Moreover, for the same slope configuration, it is possible for progressive failure to evolve.

The tensile state dominated at the surface but evolved with increasing depth, so that the shear state dominated at

the toe or in the deep part of topplings. This indicates that under earthquake load the topplings may exhibit both surface dumping and deep-seated sliding. Behind the crest of the slope, tensile failure occurs and dominates deformation by bending and dumping. Moreover, from the above analysis of acceleration propagation characteristics and displacement features, it could be observed that toppling deformation decays from behind the slope crest to the toe, and at the slope surface displacement is the highest; the resulting earthquake-induced progressive failure is correlated generally with significant variation of earthquake propagation effects along the slope (Figs. 7, 8, 10). It should be noted that displacement of the toppling under earthquake load at the toe is <0.1 m, but >0.2 m at the crest, and deformation increased with the increasing Arias intensity. So the crest and slope surface deformation is much more intense. The strongest Wenchuan input was used as an example. The plasticization zones are close to the shallow surface of the slope, because under strong motion, the propagation effects showed mainly tensile failure on the ground surface, and slope deformation amplification became obvious, especially at the crest and

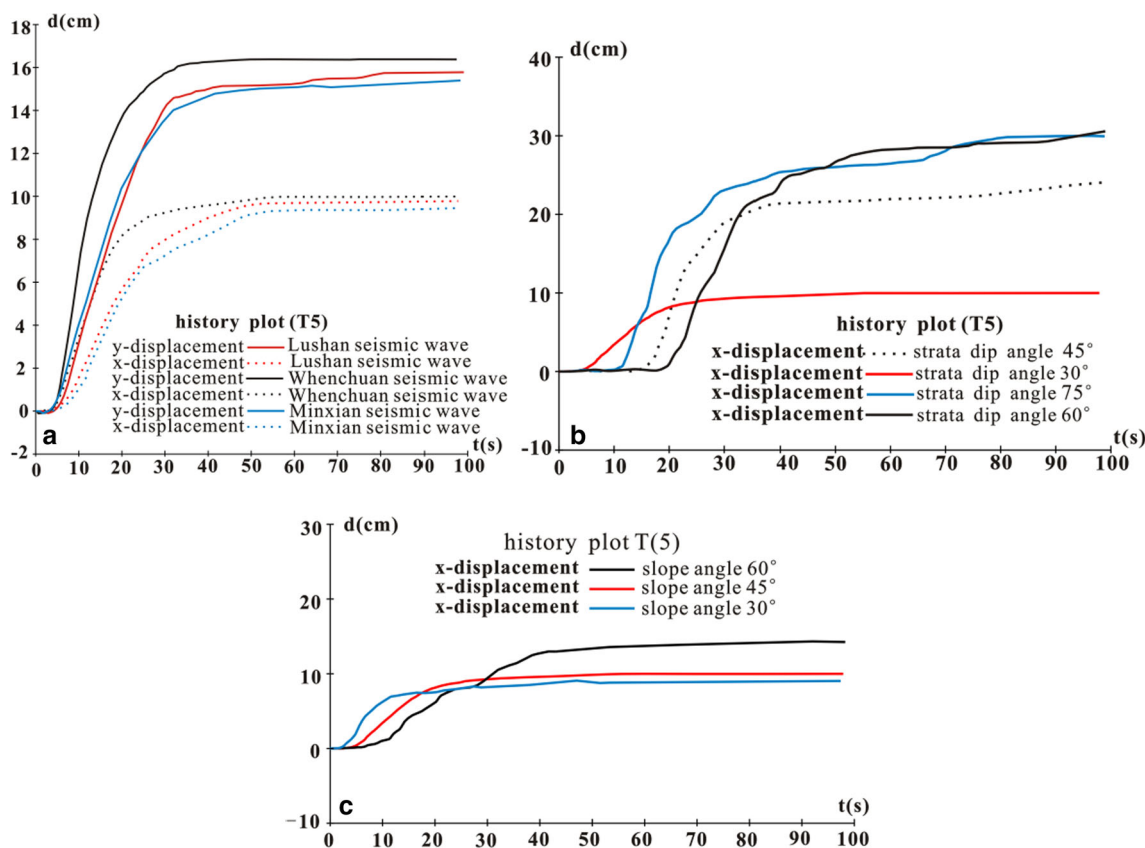


Fig. 8 Monitoring location T5 displacement history in the slope configuration (a slope configuration different earthquake_45_45; b slope configuration Wenchuan_45_different strata dip angle; c slope configuration Wenchuan_different slope angle_45)

the toe of the slope. The rock mass is relatively at a higher strength than soil, so under earthquake motion, the plasticization zones occur along the surface, possibly with some in the flat areas. Earthquake simulation of slopes is a complex topic, and maybe in some sense the DEM software is not insufficient for such a difficult problem.

Earthquake-induced toppling failure mode

It can be observed in Figs. 9 and 11a–d that, for the 30° slope angle configurations, the tensile zone evolves behind the crest toward the slope toe, moreover, failure modes dominate at the slope surface. For the Wenchuan_30_30 and Wenchuan_30_45 slope configurations, there is slight deformation at the slope toe. For the Wenchuan_30_60 slope configuration, deformation occurs at the slope surface with dumping and bending. For the Wenchuan_30_75 slope configuration, the crest area presents a wide range of tensile states, and tensile deformation dominates.

For the 45° slope angle configurations, the tensile zone evolves mainly on the crest and the upper part of the slope; moreover, failure modes dominate in these locations. Deformation is more intense than for the 30° slope angle.

For the Wenchuan_45_30 and Wenchuan_45_45 slope configurations, deformation develops at the slope surface. The rock layer bends and dumps toward the free face. For the Wenchuan_45_60 and Wenchuan_45_75 slope configurations, deformation dominates at the crest and is more widespread. For the Wenchuan_45_75 slope configuration, a shear state occurs at the toe of the slope. This configuration may develop into a composite deformation mode of tension fractures at the top and sliding at depth (Figs. 9, 11e–h).

For the 60° slope angle configurations, the tensile zone ranges widely on the slope crest and slope surface; moreover, tension fractures dominate as failure modes at the crest, while the deep part has a development trend. The top part deforms by toppling, and causes downward bending of the rock layers toward the toe. For the >45° slope angle configurations, deformation becomes progressively worse. The crest dumps and deforms obviously toward the free face in front of the slope in the Wenchuan_60_75 slope configuration (Figs. 9, 11i–l).

These results demonstrate that earthquake-induced progressive failure in topplings is mainly controlled by topographic and geologic features.

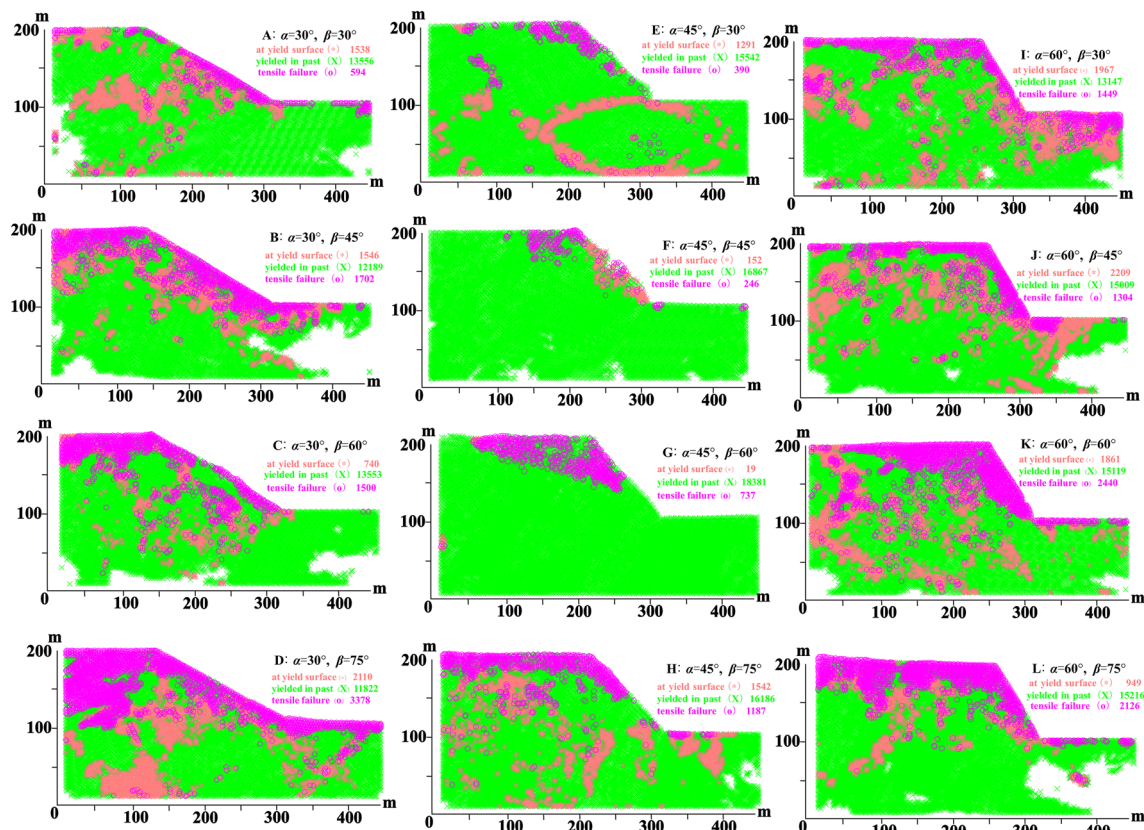


Fig. 9 Plot of the plasticity-indicators for shear and tensile failure for 12 slope configurations under the Wenchuan earthquake wave

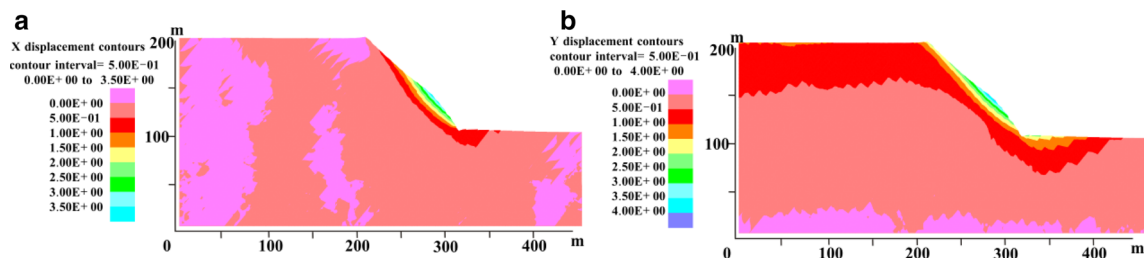


Fig. 10 Displacement contour under Wenchuan earthquake wave in slope configuration Wenchuan_45_45

Discussion

Applicability

In this study we discussed stress–strain effects, PGA propagation effects, and earthquake-induced failure modes of topplings, from a geological engineering perspective. The DEM (UDEC 4.0; Itasca 2004) is particularly suitable for simulating the response of jointed rock masses subject to either static or dynamic loading. This study is aimed at near-field earthquake motions. The Rayleigh damping selected is accurate because a lateral infinite medium was reproduced according to the quiet boundary developed by Kuhlemeyer and Lysmer (1973), in this

assumption, fewer boundary reflections waves are generated within the model. The input natural earthquake wave evaluated the possible role of earthquake propagation and deformation-failure mechanisms in earthquake-induced toppling slopes, and could be taken into account in the construction of predictive scenarios of earthquake-induced slope movements. Furthermore, numerical simulations showed that the kinematic failure modes derived from analysis of structural data and displacement patterns were reasonable. We recognize that three inputs are not sufficient for discussing such a complicated feature, as the inputs contain different spectrum accelerations from low to high, and inputs near the study area are difficult to obtain. In further studies we would collect more inputs and do

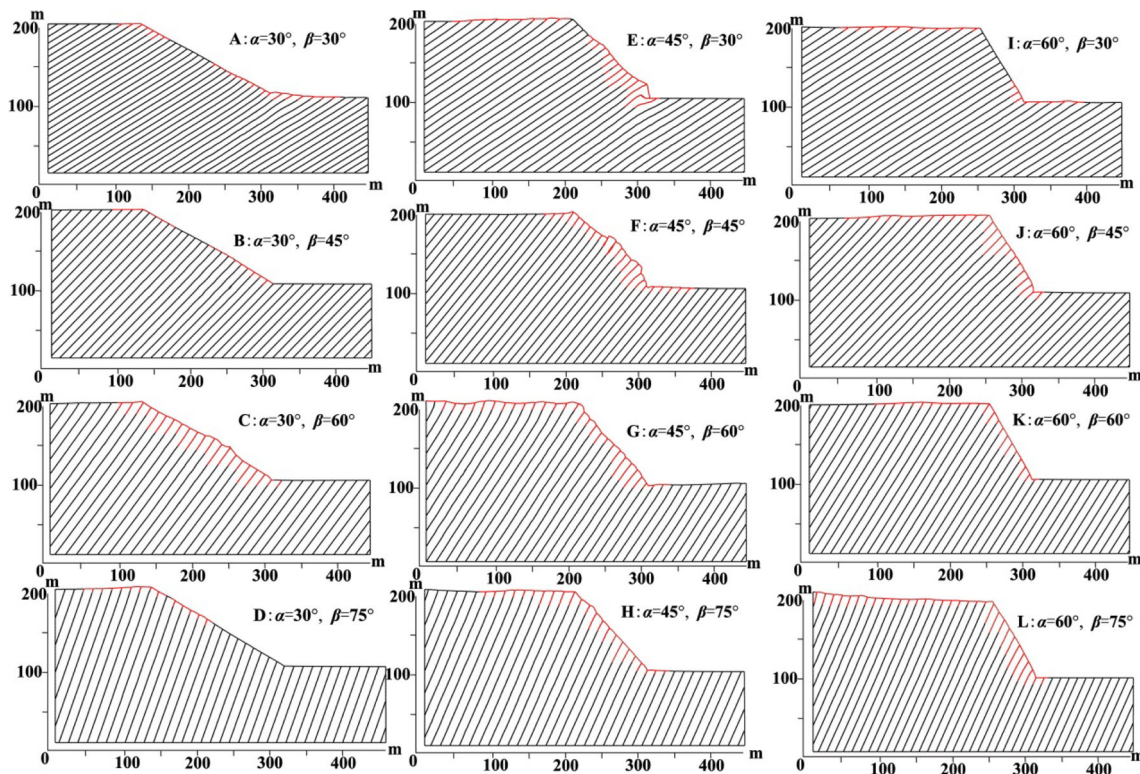


Fig. 11 Failure mode of toppling under Wenchuan earthquake wave for 12 slope configurations

more work to thoroughly analyze the subject. It must be noted that the numerical model is simplified and conceptual and the other joints are not considered; therefore, the details might be different in reality. Nevertheless, the general failure mechanism in the simulation results is not sensitive to the input parameters, as shown by the basic sensitivity analysis.

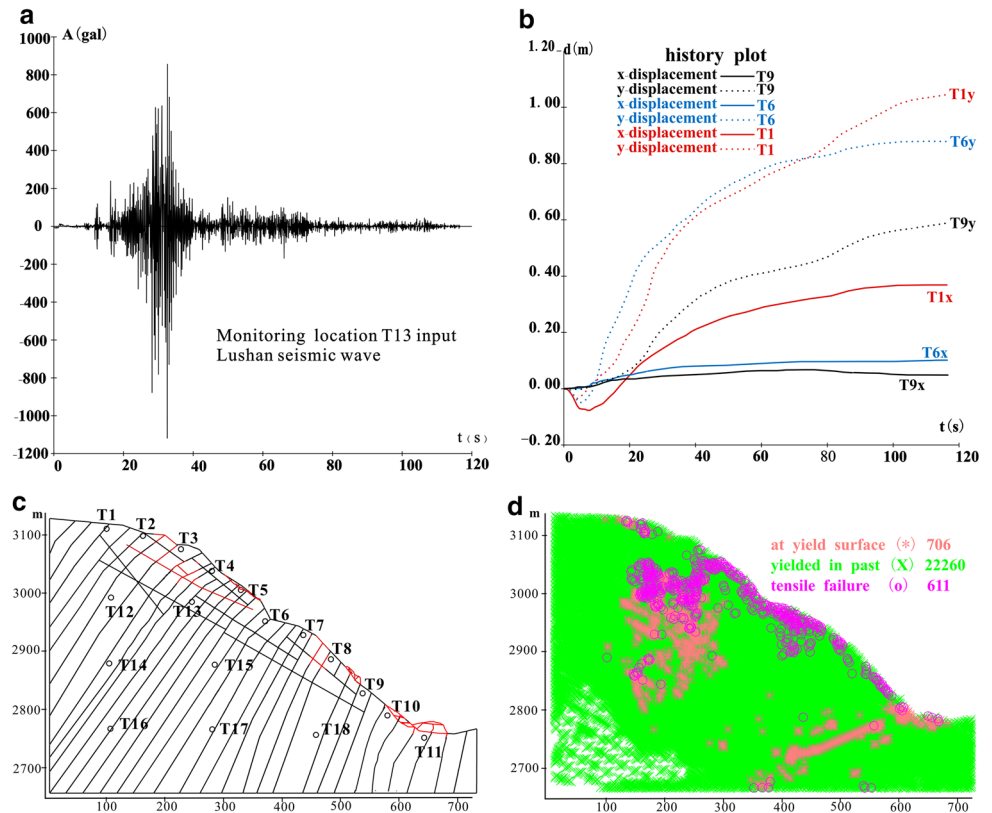
A case study

In general, the toppling here mainly presents flexural deformation. But the toppling mechanism under static load has been studied by the authors (Zhang et al. 2015), and if the design joints intersect with the strata, it should be easy to generate toppling. The presented numerical study here demonstrates that toppling geometries and their strata dip angles significantly control earthquake response and deformation. If other joints exist, the slope is more prone to deform along joints that intersect with the strata under earthquake load compared with static loads.

The toppling at the Cihaxia hydropower station in northwest China was numerically studied under the Lushan earthquake load, based on a previous study (Zhang et al. 2015). The rock joints and strata were considered. Rock and soil physical and mechanical parameters were obtained experimentally (Tables 1, 2). Figure 12a shows that the PGA at the crest reached nearly 1200 Gal, three times more

than input. Moreover, vertical displacements (y) are larger than horizontal displacements (x), and displacements decayed from the crest to the toe (Fig. 12b). The final deformation in multigroup joints exhibits tension cracks at the upper part of the slope that extend to greater depths. The loose toppled rock mass of the slope is susceptible to failure, and damage is greater near the surface. In the central part, tensile failure develops only on the slope surface. At the toe of the slope and deeper inside the slope, a shear zone evolves (Fig. 12c, d). This suggests two potential slip surfaces are critical to toppling failure evolution: surface collapse and deep landslide. This was the case in the slope under the modeled earthquake wave. Swelling and bulging occur at the toe of the slope. A rupture surface linked with tensile cracks at the trailing edge did not form inside the slope. Under the Lushan earthquake conditions (M_s 7.0, peak values of E-W 400.2 Gal and U-P 242.4 Gal, and acceleration frequency spectrum 0.02–7 Hz), the slope is basically stable. On some part of the slope surface, loose unstable rock forms and the kinetic process presents as toppling. Compared with the static load condition, under earthquake load, a much greater range of tensile deformation failure evolves at the crest and generates a shear deformation zone at the slope toe and in the deeper part of the slope. Under these conditions, the toppling may experience a much greater range of toppling.

Fig. 12 Numerical simulation results of toppling in Cihaxia hydropower station (a monitoring location T13 acceleration Time-history; b part of the monitoring location displacement history; c the slope mode and deformation condition; d plasticity-indicators for shear and tensile failure zone, the numbers in the legend keys indicate the size of plastic zone)



The UDEC 4.0 DEM analysis results (Itasca 2004) are in good agreement with those available in the literature (Bozzano et al. 2011; Pal et al. 2012) and indicate that, for the considered amplitude and frequency values of the input dynamic loads, the presence of bedrock mainly affects the earthquake response of the slope, while the effect on the horizontal topographic propagation factor is not relevant. These results are due to the contribution of the stratigraphic effect to propagation, which in turn depends on the ratio between the frequency of the input dynamic load and the natural frequency of the bedrock. Vertical displacement is larger than horizontal displacement in topplings, in contrast to earth slopes. As a result of the complex geologic conditions, deformation in the toppling slope is mainly dumping and bending from the crest toward the free face.

Further numerical analysis will be carried out by a more extensive parametric study, to investigate in greater detail the role of: (a) frequency analysis of the earthquake inputs; (b) the fundamental resonance frequency of the toppling; and (c) the geologic setting of the slopes determined by considering different stratigraphic conditions.

Comparison with conventional pseudostatic approach

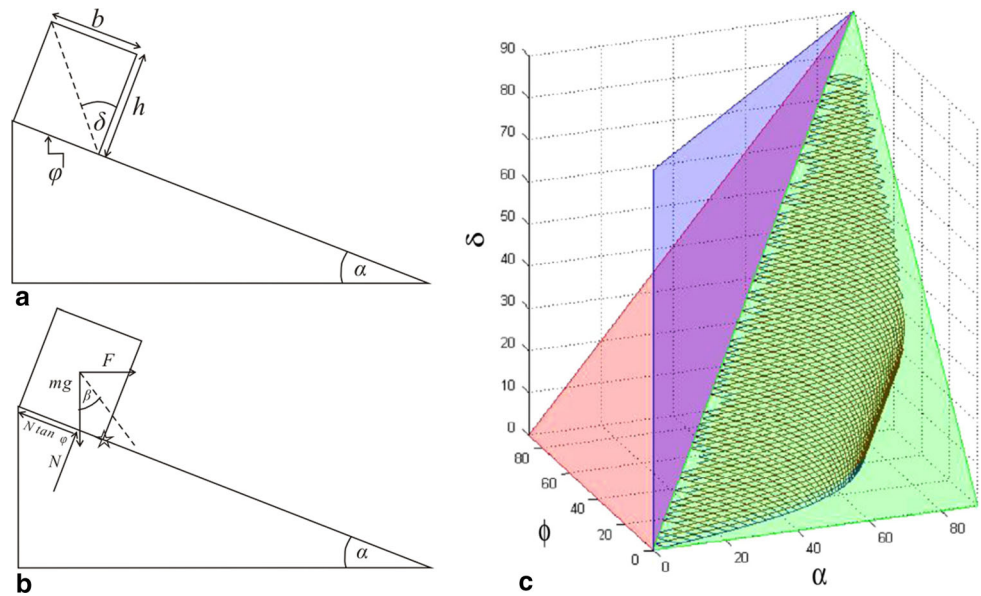
The calculated seismically induced permanent displacement is a useful design index to indicate potential damage

to a slope during an earthquake. Based on the Newmark method, some in the literature studied earthquake-induced slope displacements using simplified sliding block analyses (Rathje and Bray 2000; Jibson 1993, 2007). A coupled analytical model that simultaneously captures the fully nonlinear response of the sliding mass and the nonlinear stick–slip sliding response along the slide plane was presented by Rathje and Bray (2000). However, the aforementioned sliding-block method was applicable to rototranslational and translational landslide mechanisms (Lenti and Martino 2013). The slope sliding displacements were much greater than toppling displacements, and toppling displacements were mainly vertical. Toppling displacements are complicated to calculate using the conventional pseudostatic approach.

A block on an incline may have four different failure modes (Fig. 13): (1) static stability; (2) downslope sliding; (3) simultaneously toppling and sliding; and (4) rotation and toppling. The failure mode is governed by the geometry of both the block and the incline angle and by the frictional resistance of their interface (Fig. 13). General necessary conditions for toppling have been documented (Goodman and Bray 1976; Sagaseta et al. 2001; Liu et al. 2008; Zhang et al. 2015).

Simple calculations and a mode chart can be used to predict the mode of failure of a block on an incline when subjected to a pseudostatic force (Yagoda and Hatzor

Fig. 13 Sign convention for block on an inclined plane model (Yagoda and Hatzor 2013). **a** General mode, and **b** with pseudostatic force F . The hinge of rotation is marked by a star (δ block aspect angle defined by the ratio of block width b and height h ; α inclination angle of the slope; and φ the friction angle of the interface between slope and block; β angle between block self-weight W and the resultant of force F and block self-weight W , namely: $\tan\beta = F/W = k$; F a pseudostatic horizontal force; k pseudostatic coefficient)



2013). The PGA of the earthquake record is converted into a pseudostatic horizontal force F acting at the centroid. Four failure mode boundaries were derived: (1) between toppling and stable modes—if $\delta < \alpha + \beta$, the block will topple, and if $\delta > \alpha + \beta$, the block will not topple; (2) between sliding and stable modes, the limiting condition for sliding is $\varphi = \alpha + \beta$; (3) between sliding and sliding + toppling modes, the limiting condition for dynamic equilibrium is $\delta = \varphi$; and (4) between toppling and sliding + toppling modes, $\tan \varphi = \frac{3 \sin \delta \cos[\delta - (\alpha + \beta)] + \sin(\alpha + \beta)}{3 \cos \delta \cos[\delta - (\alpha + \beta)] + \cos(\alpha + \beta)}$; any combination of these angles will determine whether the block will topple or not.

On the basis of the aforementioned pseudostatic method, when $\varphi = 36^\circ\text{--}45^\circ$ and the strata dip angle $= 90^\circ - \delta$, conditions are comparable with the failure modes in Fig. 12: (1) if $\delta < \alpha + \beta$, $\tan \delta = b/h = k$, and $\tan \beta = F/W = k$, where k is the pseudostatic coefficient, toppling occurred with increasing k and decreasing δ ; (2) toppling also occurred with increasing strata dip angle and slope angle α . The pseudostatic method generally provides a conservative estimate. However, earthquake-induced toppling is complicated, and joint patterns significantly influence the seismic response, as they control seismic wave polarization and ellipticity close to the main joints. The UDEC 4.0 DEM method (Itasca 2004) used in this paper can solve this problem. The DEM numerical simulation results (Fig. 12) compare well with the aforementioned pseudostatic method. The failure presents topple and sliding + toppling modes.

Several issues regarding earthquake-induced toppling remain to be investigated. For example, the amplification effects of inputs from an engineering seismology point of

view, as well as the calculation of earthquake-induced toppling stability, are not explicitly described in this paper.

Conclusions

This numerical study described the influence of interactions between earthquake waves and topplings on inducing slope acceleration propagation effects and deformation failures. Different earthquake Arias intensities, slope geometric features, and stratigraphic settings were considered. On the basis of the calculation and analysis above, the following preliminary conclusions are reached.

1. Under strong motion, the acceleration propagation effect of topplings can be described as follows: the vertical and horizontal acceleration propagation factors increased with increasing slope height, reaching maximum values at the crest, and the horizontal acceleration propagation factor is much greater than the vertical. At the same elevation, the horizontal and vertical acceleration propagation factors increased from the interior to the free face of the slope. Moreover, for the same slope configuration, the acceleration propagation factors increased with increasing earthquake Arias intensity.
2. The necessary conditions for earthquake-induced toppling were discussed, and the UDEC 4.0 DEM method (Itasca 2004) and a conventional pseudostatic approach were compared. Under strong motions, the displacement response inside topplings can be described as follows: slope displacements increased with increasing slope height and increasing distance from behind the

crest area to the slope free surface. With increasing input Arias intensity, slope displacement accumulates gradually, and permanent displacement occurs in some parts of the slope. Both the horizontal displacement (x) and vertical displacement (y) increased, but vertical displacement is greater than horizontal. Slope displacement increased with increasing strata dip angle and slope angle.

- Under strong motions, a tensile state dominated at the surface of the slope but evolved with increasing depth, and a shear state dominated at the toe or in the deep part of topplings. The earthquake response effect also changes with the strata dip angle and slope angle.

This study demonstrates that the progressive failure of topplings becomes more intense with increasing slope angle, strata dip angle, and intensity of the applied dynamic input. Furthermore, these findings agree with the disequilibrium conditions that could be reached according to an ultimate-limit state criterion. Tensile failure develops at the slope surface, and a shear zone evolves at the toe and deeper inside the slope. In this regard, the deformation mode of topplings may develop into a composite of tension fracture at the crest and sliding at depth. Compared with the static scenario, under earthquake load, tensile deformation evolves over a much greater area at the crest and develops a shear zone at the toe and in the deeper part. This causes a broader range of deformation inside the slope.

Acknowledgments This study was sponsored by the Ministry of Science and Technology of China (No. 2012BAK10B02), National Natural Science Foundation of China (Nos. 41372374 and 41102165) and Project of China geological survey (No. 2120114035501). The authors express their sincere thanks to the anonymous reviewers and the editor for their invaluable help and guidance throughout this research.

References

- Alzo'ubi AK, Martin CD, Cruden DM (2010) Influence of tensile strength on toppling failure in centrifuge tests. *Int J Rock Mech Min Sci* 47:974–982
- Ashford SA, Sitar N, Lysmer J, Deng N (1997) Topographic effects on the earthquake response of steep slopes. *Bull Seismol Soc Am* 87:701–709
- Babiker AFA, Smith CC, Gilbert M, Ashby JP (2014) Non-associative limit analysis of the toppling-sliding failure of rock slopes. *Int J Rock Mech Min Sci* 71:1–11
- Bird JF, Bommer JJ (2004) Earthquake losses due to ground failure. *Eng Geol* 75:147–179
- Bobet A (1999) Analytical solutions for toppling failure. *Int J Rock Mech Min Sci* 36(7):971–980
- Bouckovalas GD, Papadimitriou AG (2005) Numerical evaluation of slope topography effects on earthquake ground motion. *Soil Dyn Earthq Eng* 25(7):547–558
- Bozzano F, Lenti L, Martino S, Montagna A, Paciello A (2011) Earthquake triggering of landslides in highly jointed rock masses: reconstruction of the 1783 Scilla rock avalanche (Italy). *Geomorphology* 129:294–308
- Bray JD, Rathje EM, Member ASCE (1998) Earthquake induced displacements of solid waste landfills. *J Geotech Geoenviron Eng* 124:242–253
- Chigira M, Wu X, Inokuchi T, Wang G (2010) Landslides induced by the 2008 Wenchuan earthquake, Sichuan, China. *Geomorphology* 118:225–238
- Goodman RE, Bray JW (1976) Toppling of rock slopes. In: *Proceedings of the specialty conference on rock engineering for foundations and slopes*, vol 2. American Society of Civil Engineering, Boulder, CO. pp 739–760
- Huang R, Zhao J, Nengpan J, Li G, Lee ML, Li Y (2013) Analysis of an anti-dip landslide triggered by the 2008 Wenchuan earthquake in China. *Nat Hazards* 68:1021–1039
- Itasca (2004) UDEC-Universal Distinct Element Code (Version 4.0). Itasca Consulting Group, Minneapolis
- Jiao Y-Y, Tian H-N, Wu H-Z, Li H-B, Tang H-M (2014) Numerical and experimental investigation on the stability of slopes threatened by earthquakes. *Arab J Geosci*. doi:10.1007/s12517-014-1509-5
- Jibson RW (1993) Predicting earthquake-induced landslide displacements using Newmark's sliding block analysis. *Transp Res Rec* 1411:9–17
- Jibson RW (2007) Regression models for estimating coseismic landslide displacement. *Eng Geol* 91:209–218
- Kokusho T, Koyanagi T, Yamada T (2014) Energy approach to earthquake induced slope failure and its application to case histories supplement. *Eng Geol* 181:290–296
- Kuhlemeyer RL, Lysmer J (1973) Finite element method accuracy for wave propagation problems. *J Soil Mech Found Div ASCE* 99(SM5):421–427
- Lenti L, Martino S (2012) The interaction of earthquake waves with step-like slopes and its influence on landslide movements. *Eng Geol* 126:19–36
- Lenti L, Martino S (2013) A parametric numerical study of the interaction between seismic waves and landslides for the evaluation of the susceptibility to seismically induced displacements. *BSSA* 103(1):33–56
- Liu CH, Jaksa MB, Meyers AG (2008) Improved analytical solution for toppling stability analysis of rock slopes. *Int J Rock Mech Min Sci* 45(8):1361–1372
- Martino S, Mugnozza GS (2005) The role of the earthquake trigger in the Calitri landslide (Italy): historical reconstruction and dynamic analysis. *Soil Dyn Earthq Eng* 25:933–950
- Mohtaramin E, Jafari A, Amini M (2014) Stability analysis of slopes against combined circular-toppling failure. *Int J Rock Mech Min Sci* 67:43–56
- Nichol SL, Hungr O, Evans SG (2002) Large-scale brittle and ductile toppling of rock slopes. *Can Geotech J* 39(4):773–788
- Pal S, Kaynia AM, Bhasin RK, Paul DK (2012) Earthquake stability analysis of rock slopes: a case study. *Rock Mech Rock Eng* 45:205–215
- Pritchard MA, Savigny KW (1990) Numerical modelling of toppling. *Can Geotech J* 27:823–834
- Rathje EM, Bray JD (2000) Nonlinear coupled seismic sliding analysis of earth structures. *J Geotech Geoenviron Eng* 126:1002–1014
- Rizzitano S, Cascone E, Biondi G (2014) Coupling of topographic and stratigraphic effects on earthquake response of slopes through 2D linear and equivalent linear analysis. *Soil Dyn Earthq Eng* 67:66–84
- Romeo R (2000) Seismically induced landslide displacements: a predictive model. *Eng Geol* 58(3/4):337–351

- Sagaseta C, Sánchez JM, Cañizal J (2001) A general analytical solution for the required anchor force in rock slopes with toppling failure. *Int J Rock Mech Min Sci* 38(3):421–435
- Saygili G, Rathje EM (2008) Empirical predictive models for earthquake-induced sliding displacements of slopes. *J Geotech Geoenviron Eng ASCE* 134(6):790–803
- Scholtès L, Donzé F-V (2012) Modelling progressive failure in fractured rock masses using a 3D discrete element method. *Int J Rock Mech Min Sci* 52:18–30
- Wasowski J, Del Gaudio V (2000) Evaluating earthquakeally induced mass movement hazard in Caramanico Terme (Italy). *Eng Geol* 58:291–311
- Yagoda Biran G, Hatzor YH (2013) A new failure mode chart for toppling and sliding with consideration of earthquake inertia force. *Int J Rock Mech Min Sci* 64:122–131
- Zhang Z, Liu G, Wu S, Tang H, Wang T, Li G, Liang C (2015) Rock slope deformation mechanism in the Cihaxia Hydropower Station, Northwest China. *Bull Eng Geol Environ* 74:943–958